Aqueous miscible organic solvent treated NiTi layered double hydroxide De-NO$_x$ photocatalysts

Adrián Pastor,[1] Chunping Chen,[2] Gustavo de Miguel,[3] Francisco Martin,[4] Manuel Cruz-Yusta,[1] Jean-Charles Buffet,[2] Dermot O'Hare,*[2] Ivana Pavlovic,[1] and Luis Sánchez*[1]

[1] Departamento de Química Inorgánica, Instituto Universitario de Nanoquímica IUNAN, Universidad de Córdoba, Campus de Rabanales, E-14014 Córdoba, España.

[2] Chemistry Research Laboratory, Department of Chemistry, University of Oxford, Oxford, OX1 3TA, UK.

[3] Departamento de Química Física y Termodinámica Aplicada, Instituto Universitario de Nanoquímica IUNAN, Universidad de Córdoba, Campus de Rabanales, E-14014 Córdoba, España.

[4] Departamento de Ingeniería Química, Facultad de Ciencias, Universidad de Málaga, Campus de Teatinos, E-29071 Málaga, España.

* Corresponding Authors:

- Prof. Luis Sánchez

  ORCID ID: 0000-0003-1115-0103

  E-mail: **luis-sanchez@uco.es**

  Tel: +00-34-957-218634

- Prof. Dermot O'Hare

  ORCID ID: 0000-0001-8054-8751

  E-mail: dermot.ohare@chem.ox.ac.uk

  Tel: +44 (0)1865 272686

Abstract

New efficient photocatalysts are required to remediate polluted urban atmospheres. We prepared a series of highly dispersed aqueous miscible organic (AMO) solvent treated NiTi layered double hydroxide (Ni_xTi-AMO-LDHs (x = 2,3)) and studied their performance in the photocatalytic abatement of NO_x gases. These photocatalysts can be prepared by a simple and scalable coprecipitation method at room temperature. Ni_xTi-AMO-LDHs (x = 2,3) have been prepared with specific N_2 BET surface areas and pore volumes up to to 492 m^2g^{-1} and 1.37 $cm^3 g^{-1}$ respectively. Under sunlight simulation, the De-NO_x performance of the conventional LDH and P25 (TiO_2) benchmarks were surpassed by 40% and 17% respectively by the Ni_xTi-AMO-LDHs. The Ni_xTi-AMO-LDHs photocatalyst also exhibited outstanding reusability and unusually low release of the toxic NO_2. The selectivity for the De-NO_x process was investigated by in situ DRIFT measurements, the high surface area and pore volume was observed to play a significant role on the adsorption of the NO_2 and N_2O_4 intermediates. The 2D character of the AMO-LDHs contributed to an enhancement in the production of radical species under illumination and reduction charge carrier recombination.

1. Introduction

Air quality in urban environments is one of the main issues marking current affairs and government policies [1,2]. The greater industrialization together with road traffic emissions are causing an increase in pollution in large cities despite the legislative measures taken [3,4]. Among the existing urban air pollutant gases, the presence of nitrogen oxides (NO_x = NO + NO_2) is of great concern because of their high toxicity and their adverse effects on the environment such as acid rain, tropospheric ozone and particulate matter formation [5,6]. Moreover, their presence in the urban atmosphere causes thousands of early deaths worldwide [7].

In recent years, photocatalysis has been shown to be a promising process to remove NO_x directly from the air (De-NO_x process) [8,9]. In contrast to the traditional catalytic reduction technologies which need high temperatures to obtain a correct De-NO_x efficacy, photocatalysis works under mild conditions (room temperature and ambient pressure) by using abundant and natural resources in the air: oxygen, water and sunlight irradiation [10]. This alternative strategy has already been applied in field trials using materials available in the commercial sector, demonstrating a potential real life application [11–13]. Commercial materials typically contain TiO_2 as a photocatalyst additive since it possesses chemical stability and a high band gap value (3.0 − 3.2 eV). Nevertheless, TiO_2 is also reported to exhibit some drawbacks such as the negligible absorption in the visible spectrum [14], poor De-NO_x selectivity (i.e. NO oxidation towards highly toxic NO_2)[15,16] or even hazardous when the powder is inhaled [17]. Therefore, research has been carried out to design alternative photocatalysts to TiO_2. Several interesting alternative De-NO_x advanced photocatalysts have been proposed lately, such as α-Fe_2O_3 [18], g-C_3N_4 [19], Fe_3O_4/*mpg*-C_3N_4 (*mpg*: mesoporous graphitic) [20],

BaWO$_4$/g-C$_3$N$_4$ [21], Cu$_{0.08}$In$_{0.25}$ZnS$_{1.41}$ [22], LaFeO$_3$-SrTiO$_3$ [23], FeOOH-Carbon quantum dots [24], WO$_3$/ZnO [25], ZnO@SiO$_2$ [26], Bi/Bi$_2$O$_{2-x}$CO$_3$ [27], Au/La-Bi$_5$O$_7$I [28], BiSbO$_4$ [29] and Bi$_2$MoO$_6$ [30], between others.

Herein we have developed a novel approach to using a family of layered double hydroxides (LDHs) as efficient De-NO$_x$ photocatalysts, working under UV light [31] or even visible light [32,33]. LDHs adopt a brucite-like structure, whose general formula may be expressed as $[(M^{z+}_{1-x}M'^{y+}_{x}(OH)_2)]^{w+}(A^{n-})_{w/n} \cdot m\text{H}_2\text{O}]$, where z is typically 2 and y can be 3 or 4, A is an n-valent anionic moiety, either organic or inorganic [34]. Among the wide variety of research fields using LDHs, photo-induced applications have been highlighted in the recent years owing to the LDH's unique properties such as easy composition variation, synthesis simplicity, uniform distribution of metal cations in the layers and oxo-bridged linkages [35]. As a result, pollutant removal [36], photodetection [37], N$_2$ fixation [38], CO$_2$ photoreduction and water splitting [39] have been reported.

Nevertheless, due to their intrinsic hydrophilicity, bulk LDHs prepared using traditional methods undergo extensive layer stacking resulting in stone-like particle aggregates of low surface area and pore volume [40]. This gives rise to a loss of the essential sites for heterogeneous photocatalytic reactions. In order to tackle this issue, bulk preparation of LDHs with particles constituted by only one monolayer or a few layers – 2D-LDHs – can be performed by LDH delamination (Top-Down Method) or from direct synthesis with controlled nucleation (Down-Top Method) [41]. However, the most efficient reported methods at room temperature often require aggressive and hazardous solvents (e.g. formamide), are time consuming (e.g. pre-intercalation of a suitable anion) and offer very low yields that prevent recovery of significant amounts of LDH [41].

Therefore it is desirable the preparation of 2D-LDHs with a satisfactory combination of mass production ability, high yield, high quality and low costs.

In order to produce large amounts of 2D-LDH samples in a much simpler way, O'Hare and co-workers devised a novel method, Aqueous Miscible Organic Solvent Treatment (AMOST) [42]. The so-formed LDH wet cake is water washed and then redispersed in an aqueous miscible organic solvent prior to the drying step, leading to so called AMO-LDHs that exhibit high dispersion and large pore volumes [40,43]. Thanks to its increased specific surface area, AMO-LDHs have been utilised as catalyst supports [44], catalyst precursors [45], flame retardant additives [46], for CO_2 capture [47] and for the thermochemical conversion of glucose to fructose [48]. However, the use of the pristine AMO product as a photocatalyst remains unexplored. Of importance, when compared to several methods reported to prepare 2D photocatalysts, AMOST procedure does not use toxic dispersants. As most of them usually contain nitrogen in their formula, the emission of NO_x gases during the photocatalysis occurs (the contrary to the desired De-NO_x process).

In this work, for the first time, we have successfully implemented the AMOST prepared 2D-LDH for its use as photocatalysts. Herein, we have studied the use of Ni_xTi-AMO-LDHs as a photocatalyst for air purification, focusing the study on the removal of NO_x gases from air. We have prepared both conventional Ni(II)/Ti(IV)-LDHs and Ni(II)/Ti(IV)-AMO-LDHs containing CO_3^{2-} as the interlayer anion (Scheme S1). There are relatively few reports of convenient and scalable methods to synthesise pure Ni_xTi LDH nanosheets (Table S1). The physicochemical properties and the photocatalytic performance of the synthesised Ni_xTi LDHs were characterised and discussed based on

parameters influencing the AMOST (i.e. metal ratio, redispersion time and temperature). We found the AMOST process increased the LDH nanosheets dispersion and the specific surface area up an unprecedented value of 492 m^2g^{-1} (Table S1). Of importance, the 2D character of samples helps to mitigate the electron/hole recombination favouring the production of radical species.

2. Materials and methods.

2.1. Chemicals

Ni(NO$_3$)$_2$·6H$_2$O, titanium isopropoxide (named as TiO^{i}Pr$_4$), Na$_2$CO$_3$, NaOH, HCl, Ethanol (EtOH) and 5,5-dimethyl-l-pyrroline-N-oxide (DMPO) were purchased from Sigma Aldrich. Methanol was purchased from PanReac AppliChem.

2.2. Photocatalysts preparation

2.2.1. Synthesis of conventional Ni$_x$Ti-LDHs (x = 2, 3).

An adapted method was followed to synthesise conventional Ni$_x$Ti-LDHs (i.e. water-treated LDHs, named as LDH-W) using the coprecipitation method [42]. 25 mmol of Ti(O^{i}Pr)$_4$ were slowly added dropwise into a 3-neck round-bottom flask containing 100 mmol of concentrated HCl under N$_2$ atmosphere. The yellowish solution thus obtained was added into a 75 mmol of Ni(NO$_3$)$_2$ aqueous solution to get a metal source with Ni:Ti = 3:1. Next, the metal source was dropped into a Na$_2$CO$_3$ aqueous solution (25 mmol) while stirring for 1 hour. During the reaction, a pH = 10 value was accurately maintained by using NaOH 4M added from an auto-titrator (Syrris, Atlas Syringe Pump). Subsequently, the mixture was stirred at room temperature for 16 h, filtered and washed

with deionised water until pH = 7. Finally, the Ni_3Ti-W sample was obtained after drying the product at 30 °C in a vacuum oven overnight (Scheme S1). Around 8 g of green solid sample, Ni_3Ti-LDH-W, was obtained (yield ~ 68%). A similar procedure was carried out to produce Ni_2Ti-W by using HCl (133.32 mmol), $Ti(O^iPr)_4$ (33.33 mmol), $Ni(NO_3)_2$ (66.66 mmol) and Na_2CO_3 (33.33 mmol).

2.2.2. Synthesis of Ni_xTi-AMO-LDHs (x = 2, 3).

For the AMO-LDH samples, the synthesis protocol is modified after the aging stage. Following a modified published procedure [43], the collected LDH product is washed with demineralised water and subsequently with 500 mL of ethanol (Scheme S1). The obtained wet solid was dispersed in ethanol (300 mL) and stirred at room temperature for 4 h. Finally, the LDH was filtered, washed with 200 mL of ethanol and dried in a vacuum oven at 30 °C overnight. These AMO-LDH samples were labelled as Ni_3Ti-E4 (Ni:Ti = 3:1) and Ni_2Ti-E4 (Ni:Ti = 2:1), where E refers to the solvent (ethanol) and 4 refers to the redispersion time (4 h).

2.2.3. Variation the AMOST parameters.

The redispersion time effect was studied over the samples with Ni:Ti = 3:1. Four additional AMO-LDH samples were synthesised for which the following redispersion times in ethanol were applied: 2, 6, 24 and 48 h. The samples were labelled as Ni_3Ti-E2, Ni_3Ti-E6, Ni_3Ti-E24 and Ni_3Ti-E48, respectively. Moreover, the temperature during the redispersion step was studied using the sample Ni_3Ti-E6 at 0 °C (Ni_3Ti-E6-0) or 50 °C (Ni_3Ti-E6-50).

2.3. Characterization of the samples

The obtained samples were characterized using the following techniques: X-ray diffraction (XRD), X-ray photoelectron spectra (XPS), Infrared (FT-IR) and UV-Vis spectroscopy; Nitrogen adsorption–desorption isotherms; Transmission electron microscopy (TEM); ICP mass spectrometry, Thermogravimetric analysis coupled with mass spectrometry (TGA-MS); Time-Resolved Photoluminescence (TRPL); Electron paramagnetic resonance (EPR).

A detailed information is provided in "Electronic Supplementary Information" (SI).

2.4. Photocatalytic activity evaluation

The ISO 22197-1 method (utilised to characterise the air purification measurement) was applied to perform the NO gas abatement photocatalytic tests. The capability of the photocatalysts to induce NO photo-oxidation was assessed in a laminar flow reactor containing a 50×50 mm quartz sample holder with 300 mg of powdered sample. The reactor was placed inside a light sealed irradiation box (Solarbox 3000e RH with Xe lamp and controlled irradiance). Samples were irradiated during the tests with artificial sunlight (irradiances of 25 and 580 W m^{-2} for UV and visible light, respectively). For each test, a flow consisted of zero air and NO (NO concentration = 500 ppb; flow rate gas = 0.37 L min^{-1}) was continuously sent to the photoreactor. The relative humidity was set to 50 ± 5 % by passing the air flow through a gas-washing bottle filled with demineralised water. A chemiluminescence analyser (Environment AC32M) measured the concentration of NO, NO$_x$ and NO$_2$ gases from the reactor. Before the irradiation period, adsorption–desorption equilibrium among photocatalysts was achieved upon

passing the air/NO flow in the dark for 10 minutes. A photocatalytic test blank (without sample) was carried to discard NO photolysis. Tests were repeated three times and the average concentration values were calculated. The obtained standard deviations were $\pm$ 0.3 ppb for NO concentration and $\pm$ 1.0 ppb for NO_2 and NO_x concentrations. The photocatalytic performance of the samples was studied regarding the NO, NO_x and S indexes (SI).

3. Results and discussion

3.1. Composition and structure

Fig. 1A and Fig. S1 show the X-ray diffraction (XRD) patterns for the synthesised Ni_xTi-CO_3 LDH samples. The XRD data exhibit the characteristic Bragg diffraction from an LDH with $R3m$ rhombohedral symmetry (JCPDS 15-0087). Specifically, the Bragg reflections at $2\theta \sim 11°$ and $23°$ correspond to the (003) and (006) basal planes respectively, while the rest of the Bragg peaks belongs to (012), (015), (018), (110) and (113) planes [49]. The basal spacing d_{003} was calculated to be 7.9 Å for the Ni_xTi-W samples (Table 1), very similar to those reported for Ni_xTi LDHs [50,51]. This value is consistent with the presence of CO_3^{2-} as interlayer anion.

The Bragg reflections are almost unaltered after the AMOST (Ni_xTi-E samples, Fig. 1A), indicating that the LDH structure is preserved [52]. Based on previous reports, the AMO solvents (i.e. ethanol) may partially enter the interlayer galleries, replacing the co-intercalated water molecules and reducing the hydrogen bonding between layers [52]. Thus, the degree of LDH layer delamination slightly increases and the layer stacking is decreased, leading to the broadness and decrease of peak intensity of the basal XRD

reflections [42,53], Fig. 1A. As a consequence the interlayer distance (d_{003}) of Ni_xTi AMO-LDHs increased up to ~ 8 Å (Table 1), this value being higher in Ni_3Ti-E4 than in Ni_2Ti-E4.

Table 1. Lattice parameters and basal spacing for the synthesised Ni_xTi LDH samples.

Sample	d_{003} (Å)	Lattice parameters (Å)		Crystal domain size (Å)	
		a	*c*	*c*-axis	*ab* plane
Ni_2Ti-W	7.89	3.07	23.67	43.6	123.5
Ni_2Ti-E4	8.01	3.08	24.02	35.2	119.7
Ni_3Ti-W	7.86	3.07	23.58	47.3	117.7
Ni_3Ti-E2	7.87	3.07	23.61	32.4	127.5
Ni_3Ti-E4	8.10	3.08	24.30	30.4	108.2
Ni_3Ti-E6	8.09	3.08	24.28	28.6	108.3
Ni_3Ti-E6-0	8.09	3.08	24.28	27.4	100.7
Ni_3Ti-E6-50	8.09	3.08	24.28	27.7	100.7
Ni_3Ti-E24	8.02	3.08	24.06	31.8	121.0
Ni_3Ti-E48	8.08	3.08	24.23	31.2	104.1

The effects of redispersion time during AMOST was studied for the Ni_3Ti-LDH samples. Samples were obtained after 2, 4, 6, 24 and 48 h of redispersion in ethanol (Fig. S1B). The Ni_3Ti-E6 sample exhibits the lowest intensity and broadest (*00l*) Bragg reflections, indicating the lowest extent of layer stacking. For redispersion times in excess of 2 h the interlayer spacing increases to a similar value *ca*. 8.09 Å, suggesting the incorporation of ethanol molecules into the LDH gallery. Redispersion temperature did not seem to be a crucial factor to boost the degree of platelet delamination (Fig S1C).

The calculated crystal domain size, using the FWHM of the *003* Bragg reflection from the Ni_xTi AMO-LDHs (Table 1), showed a significant diminution of the domain length from 47.3 to 28.6 Å with increasing dispersion time from 0 to 6 h in ethanol, indicating a

less layer stacking degree of the sheets. In this regard, the least crystal domain size is reached in the Ni_3Ti-E6 sample. Conversely, the crystal domain size along in the *ab* plane remained nearly constant for all the samples. When the redispersion time was longer than 6 h, the d_{003} parameter remained almost unaltered, which would suggest that the optimal dispersion time in the AMOST was 6 h.

ATR spectra show the characteristic bands for LDH materials (Fig. 1B) [54]. Specifically, a broad band at ca. $3350\,cm^{-1}$ is ascribed to the stretching mode of hydrogen-bonded OH arising from hydroxyl groups in the layer and the water molecules in the interlayer spacing. The bending mode of the interlayer water molecules is seen at $1638\,cm^{-1}$, Fig. 1B. The vibration mode v_3 of the interlayer carbonate anions appears split into two bands at 1462 and $1356\,cm^{-1}$. Indeed, this interlayer restricted symmetry makes the v_1 carbonate mode to show a band at $1050\,cm^{-1}$. The spectra were similar for all the samples. Additionally, for samples on which water molecules are almost completely replaced by ethanol molecules (Ni_2Ti-E4 and Ni_3Ti-E6 samples, Table 2), new low intensity bands appeared at 2974 and $1093\,cm^{-1}$ and the band at $1050\,cm^{-1}$ noticeably increased, Fig. S2. In order to reveal the origin of these bands and discard possible impurity phases, the ATR spectra of other related compounds TiO_2, $Ni(OH)_2$ (most common impurities) and ethanol were recorded (Fig. S3). The comparison of the spectra indicates that these new bands should correspond to the presence of ethanol molecules adsorbed/incorporated in AMO-LDH. Slight shifts in the wavenumber of these bands might be a consequence of the different vibration behaviour between free ethanol and that incorporated into the AMO-LDH galleries.

X-ray photoelectron spectroscopy (XPS) was used to analyse the Ni_xTi-LDH surface in order to probe the oxidation states of Ti and Ni. C 1s signal at 284.8 eV, was used as internal charge shift correction. No significant differences between samples were found in their XPS spectra. As way of example, the X-ray photoemissions of Ni_3Ti-W are shown in Fig. S2. The Ni $2p_{3/2}$ signal at 855.6 eV corresponds to Ni^{2+} hydroxide (Fig. S4A). Fig. S4B shows the high resolution Ti 2p region. The Ti $2p_{3/2}$ signal has been deconvoluted in two resonances set at 459.2 and 457.7 eV, and the corresponding to $Ti2p_{1/2}$ at 464.7 eV and 463 eV respectively, which have been proposed to correspond to the contributions from Ti^{4+} ions in tetrahedral and octahedral coordination, respectively [55]. This is indicative that at the surface, some Ti^{4+} ions may have migrated out of the LDH layer network, possibly due to the high electrical charge of Ti^{4+}. No evidence for any Ti^{3+} species was found in the samples, although these have been reported in Ni_xTi-LDHs synthesised by other methods [56]. The C 1s XPS region shows contributions corresponding to the adventitious hydrocarbon, –CO, and –COO– groups at 284.8, 286 and 288.6 eV respectively (Fig. S4C). Finally, the O1s peak has been deconvoluted in three peaks at 529.5, 531.1 and 532.5 eV, which have been assigned to lattice oxygen in metal oxides (M-O-M), hydroxyl groups (M-O-H) and adsorbed water (H-O-H), respectively (Fig. S2D) [57].

All samples showed similar TGA profiles, characteristic of LDHs [50]. The derivative of the TGA curves are depicted in order to investigate the mass losses in more details (Fig. S5). Ni_3Ti-W exhibits two mass loss events at 107 and 285 °C (P1 and P2 peaks, respectively). The first one is ascribed to the removal of adsorbed and interlayer water, while the second one is due to both carbonate decomposition and dehydroxylation of LDH [58]. For Ni_2Ti-W, both mass losses appeared shifted to lower temperature than the

Ni$_3$Ti-W sample (Fig. S5B), which could be a consequence of some structural disorder in the LDH network due to its higher Ti^{4+} cations content. When the AMOST was applied (Ni$_x$Ti-E samples), the P1 event occurred at a lower temperature suggesting the presence of both ethanol and water molecules. Moreover, the temperature onset of the P1 event shifted depending on the AMOST redispersion time (Fig S5D), appearing at the lowest temperatures for the Ni$_3$Ti-E4 and Ni$_3$Ti-E6 samples. Beyond 6 h of redispersion time in the AMOST, the P1 event shifted to higher temperature, indicating that the optimal ethanol substitution was achieved at 6 h. The lower desorption temperatures at the P1 event are indicative of weaker interactions between sorbates and metal hydroxide layers, and the higher dispersion of the platelets. Similarly, the P2 event also underwent similar behaviour in the AMO samples.

LDH composition was calculated by using the data from TGA and ICP-MS techniques (in all cases carbonate anions were assumed to balance the layer positive charge, Table 2). Good agreement was found between the experimental values and the theoretical metal ratios in the initial solution. TGA-MS studies corroborates that water molecules in LDH structure are partially replaced by ethanol when the AMOST was performed (Fig. S6). Water signal (m/z =18) decreased (Fig S6A) and the ethanol signal appeared in Ni$_3$Ti-E samples (Fig S6B). The P1 events from the derivative curves of the samples were deconvoluted to calculate the amounts water and ethanol (Fig S6C, D) present. The estimated quantities of ethanol in the samples (Table 2) correlated well with the interlayer stacking and crystal domain size inferred from the XRD data. Thus, those samples with a higher ethanol content (Ni$_3$Ti-E6 samples) exhibit the highest interlayer distance (d$_{003}$) and, because of the delamination effect, lower crystal domain size.

Table 2. Chemical properties for the synthesised Ni_xTi LDH samples: metal content and ratio; formula and band gap energy value.

Sample	% Atomic		Atomic ratio	Formula	Band gap (eV)
	Ni	Ti	Ni/Ti		
Ni_2Ti-W	0.55	0.23	2.37	$[Ni_{0.71}Ti_{0.3}(OH)_2](CO_3)_{0.3} \cdot 0.91\ H_2O$	2.56
Ni_2Ti-E4	0.55	0.22	2.47	$[Ni_{0.71}Ti_{0.29}(OH)_2](CO_3)_{0.29} \cdot 0.09\ H_2O \cdot 0.37\ EtOH$	2.94
Ni_3Ti-W	0.65	0.21	3.14	$[Ni_{0.77}Ti_{0.23}(OH)_2](CO_3)_{0.23} \cdot 0.92\ H_2O$	2.54
Ni_3Ti-E2	0.65	0.21	3.04	$[Ni_{0.75}Ti_{0.25}(OH)_2](CO_3)_{0.25} \cdot 0.19\ H_2O \cdot 0.27\ EtOH$	2.96
Ni_3Ti-E4	0.63	0.21	2.96	$[Ni_{0.75}Ti_{0.25}(OH)_2](CO_3)_{0.25} \cdot 0.17\ H_2O \cdot 0.31\ EtOH$	2.91
Ni_3Ti-E6	0.60	0.18	3.26	$[Ni_{0.77}Ti_{0.23}(OH)_2](CO_3)_{0.23} \cdot 0.01\ H_2O \cdot 0.38\ EtOH$	2.94
Ni_3Ti-E6-0	0.61	0.18	3.31	$[Ni_{0.78}Ti_{0.23}(OH)_2](CO_3)_{0.23} \cdot 0.04\ H_2O \cdot 0.40\ EtOH$	2.96
Ni_3Ti-E6-50	0.60	0.18	3.30	$[Ni_{0.77}Ti_{0.23}(OH)_2](CO_3)_{0.23} \cdot 0.04\ H_2O \cdot 0.39\ EtOH$	2.96
Ni_3Ti-E24	0.57	0.18	3.18	$[Ni_{0.76}Ti_{0.24}(OH)_2](CO_3)_{0.24} \cdot 0.08\ H_2O \cdot 0.35\ EtOH$	2.92
Ni_3Ti-E48	0.65	0.21	3.14	$[Ni_{0.76}Ti_{0.24}(OH)_2](CO_3)_{0.24} \cdot 0.14\ H_2O \cdot 0.23\ EtOH$	2.88

3.2. Morphology and textural properties of photocatalysts

Different morphologies were found for the Ni_3Ti-W and Ni_3Ti-E samples (Figs. 2 and S7). Ni_3Ti-W sample (Fig. 2A, S7A and S8A) consisted of irregular particles with severe aggregation produced by the strong interactions between the metal hydroxide layers, interlayer anions and water molecules. In contrast, flower-type particles constituted by corrugated nanosheets were observed after the AMOST (Fig. S7B, C, D E and F). The highest dispersion of nanosheets is observed for treatment times longer than 2 h. For the Ni_3Ti-E samples optimal delamination was observed after at 6 h. Thus, the observed thickness of nanosheets decreased from 4 − 5 nm of sample Ni_3Ti-E2 to 1 − 3 nm of sample Ni_3Ti-E6. The morphology transformation is attributed to the AMOST effect, specifically the ethanol displacing bound water from the LDH surface and reducing the propensity of hydrogen bonding. Some insertion of ethanol molecules into the LDH

interlayer spacing also takes place [40], the net effect being a boost of the metal hydroxide layers exfoliation. Similar observations were found with Ni_2Ti-E samples (Fig. S8). The temperature on the redispersion step made no appreciable differences to the sample dispersion Ni_3Ti-E6 (Fig. S9).

In order to learn more about the pore structure and surface areas of the samples, they were investigated by N_2 adsorption-desorption measurements (Fig. 3, S10, S11 and S12). According to IUPAC classification, the isotherm shape of Ni_3Ti-W and Ni_2Ti-W samples were characteristic of a type II isotherm with a H2-type hysteresis, which indicates the presence of narrow-neck porosity with wide bodies. These pore types should be a consequence of the huge interparticle aggregation, as observed by TEM. This microstructure was altered in the AMO samples. Now, a IV type isotherm with a H3 hysteresis loop is observed for all of them (Figs. 3B, S10 and S11B), this is in agreement with those reported for other AMO-LDHs [43]. This pore structure is associated to slit-shaped pores arising from the sheet-like morphology as observed in TEM images.

The redispersion time effect had a clear influence in the specific surface area and pore volumes. The corresponding values mesuared for Ni_3Ti-E2, Ni_3Ti-E4, Ni_3Ti-E6, Ni_3Ti-E24 and Ni_3Ti-E48 samples are shown in Fig. 3C. The maximum values are reached after ethanol dispersion for 6 h (492 $m^2\ g^{-1}$ and 1.37 $cm^3\ g^{-1}$, respectively). This is consistent with the TEM observations that showed a higher amount of thin nanosheets in Ni_3Ti-E6 sample. The Ni:Ti ratio seemed to affect the AMOST effectiveness (Table S2), ethanol was less effective at dispersing Ni_2Ti platelets compared to Ni_3Ti platelets, the N_2 BET surface area increased by 0.25 and 3 times for Ni_2Ti-E4 and Ni_3Ti-E4, respectively. It is thought the greater layer charge density has made it more difficult for the ethanol to delaminate

the platelets as confirmed by the XRD data. Ni_3Ti-E6 showed the highest surface area and pore volume demonstrating that room temperature is the optimum choice to obtain the highest degree of delamination (Table S2).

By analysing the pore size distribution for different redispersion times, it was found that the specific surface area boost came from the increase of the mesoporous and macroporous pore regime (Fig. S13). Specifically, pores in the region $6 - 13$ nm and $20 - 40$ nm were generated for all Ni_3Ti-E samples, except for Ni_3Ti-E2, suggesting that the delamination, by the AMOST process, has not totally been completed for this sample. The Ni_3Ti-E6 porosity increased in the $4 - 5$ nm pore size region. Because its higher degree of delamination, the significance of this small pore diameter could be associated to occurrence of a high number of slit-shaped pores between the exfoliated nanosheets. In fact, both the porosity in the $4 - 13$ nm range and the pore volume increased with the specific surface area (Fig. S13A).

3.3. Optical properties

The diffuse reflectance UV–Vis absorption spectra of Ni_3Ti-W and Ni_3Ti-E4 samples are plotted in Fig. 4A. Two clear absorbances were observed: bands between 200 and ~400 nm were ascribed to the ligand-to-metal charge transfer for Ti^{4+} in an octahedral environment, while the broad band in the region of 600-800 nm can be assigned to d-d transitions for the Ni^{2+} located in the layers [59]. This absorbance in the visible spectrum region gives rise to a characteristic green colour observed for the Ni_xTi LDH-W samples (Fig S14). Remarkably, the sample absorbance in this region was decreased when the AMOST was performed, probably caused by the enhanced LDH particle dispersion (Figs. S15A, B). Band gap values were calculated by plotting the

transformed Kubelka-Munk function versus the photon energy (Figs. 4B and S15C, D). The Ni$_3$Ti-W sample showed an estimated band gap of around 2.5 eV (Table 2), a similar value to that reported for previously reported NiTi-LDHs [56,59]. This value increased to ~ 0.4 eV for all the Ni$_x$Ti AMO-LDH samples. Analogous results were observed for the Ni$_3$Ti samples following different redispersion times (Fig. S15C). After the redispersion process the Ni$_3$Ti-LDH nanosheets are typically only a few layers thick. Similar to that observed for 2D layered semiconductors, the electronic band structure changes with the number of layers; band gap increasing with decreasing thickness because of confinement effects [60].

3.4. De-NOx performance assessment

The synthesised compounds along with the benchmark TiO$_2$ P25, used as standard for comparison purposes, were subjected to photocatalytic tests to evaluate their activity for the NO gas removal. Figure 5A shows the NO$_x$ gases concentration values recorded for the Ni$_3$Ti-E4 photocatalyst in a typical De-NO$_x$ test. During the first 10 minutes, under dark conditions, the simulated polluted atmosphere is flowed through the photoreactor and the concentration of the gases remains constant. Upon light irradiation the NO gas concentration rapidly drops due to the onset of photocatalytic processes. On the surface of the sample, reactive oxygen species (ROS) are produced and these are responsible of the photochemical oxidation of the NO [8,61,62], which may be briefly summarised as follows: NO $\rightarrow$ NO$_2^-$ $\rightarrow$ NO$_2$ $\rightarrow$ NO$_3^-$. This process is fully selective when all nitrogen gases are removed as nitrite and/or nitrate species. After 60 minutes of light irradiation, the lamp is turned off and the photocatalytic process stops. After 10 minutes the gas concentration recovers the original values. The De-NO and De-NO$_x$ performances for the

Ni$_3$Ti-W and Ni$_3$Ti-AMO-LDH samples with different ethanol redispersion times is depicted in Figs. 5B, C. We observed that the photocatalytic performance is closely related with the specific surface areas of the samples. Ni$_3$Ti-W showed the lowest conversion figures (De-NO$_x$ activity $\sim$ 18 %), much lower than the AMO samples (De-NO$_x$ activity > 50%). AMOST promotes delamination, increase in specific surface area, leading to an increase in exposure of the reactant gases to the photocatalytic centres on the LDH surface. The Ni:Ti ratio does not seem to be an important factor in determining photocatalytic activity, Ni$_2$Ti-E4 and Ni$_3$Ti-E4 both with surface areas $\sim$ 312 m^2 g^{-1} exhibit similar De-NO activity (Fig. S16A). Ni$_3$Ti-E6 samples, having the highest surface area, exhibited outstanding De-NO conversion of about 63 %, and superior to that observed for the TiO$_2$ P25 (57 %) reference sample (Figs. 5B and S16B).

More interestingly, the Ni$_x$Ti-AMO-LDH samples stand out in their ability not to emit NO$_2$ gas, an intermediate appearing in the sequential photochemical oxidation of NO. This is a key factor for successfully applying these materials within an urban environment because NO$_2$ is much more hazardous [63]. In order to assess this, the estimated selectivity (S) index is shown in Fig. S17. Most Ni$_x$Ti-AMO-LDHs showed S values of $\sim$ 94 %, higher than LDH-W (~80 %) and TiO$_2$ P25 (72 %). This result would be related with an enhanced adsorption ability towards NO$_2$ for the Ni$_x$Ti-AMO-LDHs due to their larger specific surface areas. In this regard, the NO$_2$ adsorption tests in darkness (Fig. S18) showed that, from an inlet value of 150 ppb of NO$_2$, a significant amount ($\sim$ 47 %) is removed over 1 hour by Ni$_3$Ti-E6. Conversely, lower amounts of NO$_2$ gas are adsorbed by Ni$_3$Ti-W and TiO$_2$ P25 (20 and 3 %, respectively). This could be due to a superior ability for Ni$_x$Ti-AMO-LDHs to adsorb NO$_2$ on the surface and then facilitate complete photocatalytic oxidation. In this sense, it has been previously reported that mesoporous networks lead
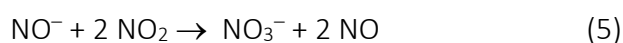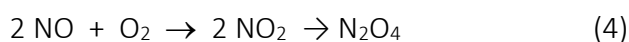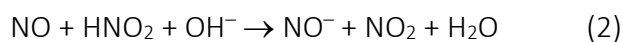
to easy accessibility of active reactive sites to the reactant molecules [64], acting as a sink on which the nitrogen oxide gases molecules are trapped [65]. Therefore, the higher mesopore volume of Ni_3Ti-E6, compared to Ni_3Ti-W, could serve to restrain the NO_2 molecules.

As a consequence, complete removal of NO_x performed by each photocatalyst (De-NO_x activity, Fig 5C) is related with its selectivity towards the Photocatalytic Oxidation (PCO) process. Thus, Ni_3Ti-E6 samples exhibit De-NO_x values around 57 %, 29 % higher than the one shown using TiO_2 P25, being comparable or even superior to those previously reported LDH De-NO_x photocatalysts (42 %, NiMgAl-LDH;[66] 50 %, ZnAl-LDH [31]; 50 %, ZnAlCr-LDH [32]; 59 %, ZnAlFe-LDH [33]. Moreover, the reusability of the Ni_3Ti-E6 and TiO_2 P25 photocatalysts was evaluated (Fig. S19). After six runs (6 hours of light irradiation), the De-NO_x activity of Ni_3Ti-E6 photocatalyst remained almost constant, producing outstanding De-NO_x performance (~58 %). Because its high surface area (492 m^2g^{-1}), there are clearly a vast number of available active sites on photocatalyst's surface to confront the oxidation of a huge amount of NO_x molecules. Thus, after each run, there are still enough active sites that remain unreacted to keep the De-NO_x performance constant. Therefore, the characteristic nitrate passivation of the surface is delayed, whose later appearance should be easily removed by using a simple water washing procedure [31–33]. However, the photocatalytic activity of TiO_2 P25 was significantly reduced (~44 %). Remarkably, the NO_2 emission was around 8 times lower for the AMO photocatalyst than for the TiO_2 P25 (Fig. S19 C, D). In summary, the NO removal efficiency and Selectivity values found for AMO photocatalysts are in line with those recently reported for advanced De-NO_x photocatalysts, Table S3.

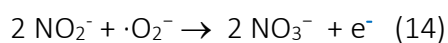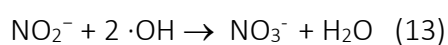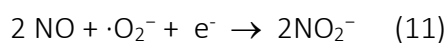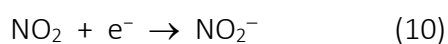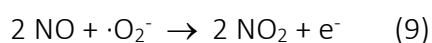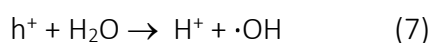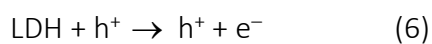## 3.5. Photocatalytic mechanism assessment

Several experiments were performed to get an insight into the photocatalytic mechanism expected for the Ni_xTi AMO-LDHs. Picosecond time-resolved photoluminescence decays (TRPL) were measured for Ni_3Ti-W and Ni_3Ti-E photocatalysts. Fig. 6A displays the time profiles at 470 nm with the best bi-exponential fits for both photocatalysts. For the samples studied, the deactivation kinetics for the excited state develop within the same time range with time constant of 6.4 and 284 ns for Ni_3TiW, 6.5 and 260 ns for Ni_3Ti-E2, and 5.13 and 562 ns for Ni_3Ti-E6 photocatalysts. The recombination kinetics of the electrons in the Ni_3Ti-E6 samples was slightly slower, which might enhance the photocatalytic activity of this compound. In parallel, EPR measurements were used to probe the reactive species involved in the photochemical process. For methanolic DMPO solutions, under light irradiation, the characteristic sextet of peaks for the trapped $\cdot O_2^-$ radical is observed for the three samples, Fig. 6B. The intensity of the signal increases in the order Ni_3Ti-E6 > Ni_3Ti-E2 > Ni_3Ti-W, being higher with the delamination degree of the sample. For aqueous solutions, the quartet of peaks DMPO-$\cdot$OH adduct is clearly observed for the Ni_3Ti-W sample (Fig. 6C). However, the signal obtained for the case Ni_xTi-E photocatalysts is more complex. Even though the mentioned quartet is shown, there are additional peaks (marked with asterisk) which precludes the existence of DMPO-$\cdot O_2^-$ adduct, which would be originated from the existence of ethanol molecules in the samples. The higher amount of superoxide detected for Ni_3Ti-E6 sample together with the slower recombination kinetics observed would be in agreement with a higher availability of electrons on the semiconductor surface. As previously reported, the 2D character of this photocatalyst facilitates the electron conduction through the surface lessening the e^-/h^+ recombination [38].

In situ DRIFTS measurements were carried out with the aim to monitor the photocatalytic removal of NO. Initially, the samples were subjected to pre-treatment and NO adsorption processes. The background spectrum was recorded before NO flow through the reaction chamber. Fig. 7A shows the spectra obtained under dark conditions for samples Ni$_3$Ti-W and Ni$_3$Ti-E6, once the background had been subtracted, after 10 minutes of NO flow. Signals corresponding to the appearance of NO$_x$ species are observed. Clear differences between both samples were found. The IR spectra indicate that NO is easily adsorbed onto Ni$_3$Ti-E6 photocatalyst surface (1070 cm^{-1}, [66,67]), presumably due its very high specific surface area. As a result, NO$^-$ and NO$_2^-$ species (1107 cm^{-1} and 838-873 cm^{-1}, [67,68]) are produced by NO disproportionation in the presence of the hydroxyl LDH groups [69]; (Eqs. (1-3)), which ultimately are oxidised to nitrate (1527 − 1577 cm^{-1}, [70,71]) (Eq. (5)). In addition, in the presence of O$_2$, NO is partially oxidised to NO$_2$ which could converted into N$_2$O$_4$ (901 cm^{-1} [68]; Eq. (4)). This last identification emphasizes the ability of Ni$_3$Ti-E6 sample to adsorb most gases. These processes are scarcely observed in Ni$_3$Ti-W because its low affinity for NO adsorption. These transformations can be summarised as follows:

$$2\ NO + OH^- \rightarrow HNO_2 + NO^- \qquad\qquad (1)$$

$$NO + HNO_2 + OH^- \rightarrow NO^- + NO_2 + H_2O \qquad (2)$$

$$NO^- + NO_2 \rightarrow NO_2^- + NO \qquad\qquad (3)$$

$$2\ NO\ +\ O_2\ \rightarrow\ 2\ NO_2\ \rightarrow N_2O_4 \qquad\qquad (4)$$

$$NO^- + 2\ NO_2 \rightarrow NO_3^- + 2\ NO \qquad\qquad (5)$$

Afterwards, the samples were irradiated by light during 60 minutes, and the amount and tipology of adsorbed species on surface change significantly. As light reachs the surface of the catalyst, the photoexcited e^- and h^+ (Eq. (6)) react with H_2O and O_2 to produce hydroxyl and superoxide radicals (Eqs. (7-8)), which promote the photochemical oxidation of NO. Thus, the spectra show now a larger number and more intense signals corresponding mainly to nitrite (843-882, 1138, 1294, 1353 and 1434 cm^{-1}, [67,68,71,72]) and nitrate species (924-1054 and 1527-1583 cm^{-1}, [66,67,70,71]), as the resulting products of the NO photo-oxidation (Fig. 7B) (Eqs. (10-14)). Consistent with its high De-NO$_x$ photoactivity, the spectra of Ni$_3$Ti-E6 are differentiated by the highest intensity of these signals, the majority assigned to NO_3^-, the final product of the PCO process. Under light irradiation, the ocurrence of NO_2 (1240 cm^{-1}, [67]) accounts from the oxidation of NO by superoxide radicals (Eq. (9)), which in turn dimerizes to N_2O_4 (1397 cm^{-1}, [69]). The identification of NO_2 and N_2O_4 on the surface is in agreement with the higher De-NO$_x$ selectivity of this photocatalyst. Thus, the retention of these molecules on surface facilitates their oxidation, decreasing their emission to the atmosphere. Interestingly, the presence of NO$^-$ bands persisted under light irradiation, more clearly for the Ni$_3$Ti-E6 sample. This evidence suggested that, similarly to that observed in the reusability tests and after one hour of light irradiation, many unreacted active sites remained available on photocatalyst's surface to react with gaseous molecules, playing the hydroxyl LDH groups a key role in anchoring NO molecules as NO$^-$, role emphasized by the large surface area exhibited by the Ni$_3$Ti-E6 sample.

Considering the above results, the primary NO oxidation reaction mechanism could be proposed as follows:

$$LDH + h^+ \rightarrow h^+ + e^- \qquad (6)$$

$$h^+ + H_2O \rightarrow H^+ + \cdot OH \qquad (7)$$

$$e^- + O_2 \rightarrow \cdot O_2^- \qquad (8)$$

$$2\,NO + \cdot O_2^- \rightarrow 2\,NO_2 + e^- \qquad (9)$$

$$NO_2 + e^- \rightarrow NO_2^- \qquad (10)$$

$$2\,NO + \cdot O_2^- + e^- \rightarrow 2NO_2^- \qquad (11)$$

$$NO + \cdot OH \rightarrow HNO_2 \qquad (12)$$

$$NO_2^- + 2\,\cdot OH \rightarrow NO_3^- + H_2O \qquad (13)$$

$$2\,NO_2^- + \cdot O_2^- \rightarrow 2\,NO_3^- + e^- \qquad (14)$$

The in situ DRIFTS spectra provides evidence for the higher efficiency of Ni_3Ti-E6 to promote the photochemical NO oxidation. The ability of Ni_3Ti-E6 to physi/chemisorb NO and NO_2 on the surface facilitates their oxidation to nitrites and nitrates, resulting a high De-NO_x selectivity.

4. Conclusions

A range of Ni_xTi-AMO-LDHs with different degrees of platelet dispersion were synthesised using the AMOST process. The redispersion time of the Ni_xTi LDHs in ethanol strongly influenced the surface area and pore volumes of the sample. Extensive nanosheets dispersions was observed after 6 h of ethanol dispersion leading to N_2 BET surface areas as high as 492 m^2g^{-1}.

Ni$_x$Ti-AMO-LDHs were found to be effective photocatalysts, they exhibited much higher De-NO$_x$ performance in comparison to the untreated LDH and the TiO$_2$ P25 benchmark producing a performance of ~58% under sunlight illumination (40 and 17% higher than conventional LDH and TiO$_2$ P25 respectively). Most importantly, the Ni$_x$Ti-AMO-LDHs photocatalysts exhibited stable photocatalytic activity after consecutives cycles, but they showed negligible emission of the toxic intermediate NO$_2$.

The key role of the specific surface area was revealed: i) the higher number of specific sites of the Ni$_x$Ti-AMO-LDHs photocatalysts provided an enhancement for the adsorption capacity for NO and especially NO$_2$ and delayed the photocatalyst pasivation; ii) the 2D character promotes a lessening of the charge carrier recombination and the increase in the radical species production. Both characteristics, with difference to TiO$_2$ P25, assist for the enhancement of the De-NO$_x$ photocatalytic process. We conclude that AMO-LDHs provide a platform approach to developing new effective and robust candidates for the photocatalytic NO$_x$ removal.

References

[1]   W.H.O. WHO, 9 out of 10 people worldwide breathe polluted air, but more countries are taking action, (n.d.). https://www.who.int/news-room/detail/02-05-2018-9-out-of-10-people-worldwide-breathe-polluted-air-but-more-countries-are-taking-action (accessed July 5, 2021).

[2]   P.J. Landrigan, R. Fuller, N.J.R. Acosta, O. Adeyi, R. Arnold, N. (Nil) Basu, A.B. Baldé, R. Bertollini, S. Bose-O'Reilly, J.I. Boufford, P.N. Breysse, T. Chiles, C. Mahidol, A.M. Coll-Seck, M.L. Cropper, J. Fobil, V. Fuster, M. Greenstone, A. Haines, D. Hanrahan, D. Hunter, M. Khare, A. Krupnick, B. Lanphear, B. Lohani, K. Martin, K. V. Mathiasen, M.A. McTeer, C.J.L. Murray, J.D. Ndahimananjara, F. Perera, J. Potočnik, A.S. Preker, J. Ramesh, J. Rockström, C. Salinas, L.D. Samson, K. Sandilya, P.D. Sly, K.R. Smith, A. Steiner, R.B. Stewart, W.A. Suk, O.C.P. van Schayck, G.N. Yadama, K. Yumkella, M. Zhong, The Lancet Commission on pollution and health, Lancet. 391 (2018) 462–512. doi:10.1016/S0140-6736(17)32345-0.

[3]   S.K. Grange, N.J. Farren, A.R. Vaughan, R.A. Rose, D.C. Carslaw, Strong Temperature Dependence for Light-Duty Diesel Vehicle NO_x Emissions, Environ. Sci. Technol. 53 (2019) 6587–6596. doi:10.1021/acs.est.9b01024.

[4]   A. Folli, S.B. Campbell, J.A. Anderson, D.E. MacPhee, Role of TiO_2 surface hydration on NO oxidation photo-activity, J. Photochem. Photobiol. A Chem. 220 (2011) 85–93. doi:10.1016/j.jphotochem.2011.03.017.

[5]   Q. Di, H. Amini, L. Shi, I. Kloog, R. Silvern, J. Kelly, M.B. Sabath, C. Choirat, P. Koutrakis, A. Lyapustin, Y. Wang, L.J. Mickley, J. Schwartz, Assessing NO_2 Concentration and Model Uncertainty with High Spatiotemporal Resolution

across the Contiguous United States Using Ensemble Model Averaging, Environ. Sci. Technol. 54 (2020) 1372–1384. doi:10.1021/acs.est.9b03358.

[6]   B.N. Duncan, L.N. Lamsal, A.M. Thompson, Y. Yoshida, Z. Lu, D.G. Streets, M.M. Hurwitz, K.E. Pickering, A space-based, high-resolution view of notable changes in urban NO$_X$ pollution around the world (2005-2014), J. Geophys. Res. Atmos. 121 (2016) 976–996. doi:10.1002/2015JD024121.

[7]   5,000 deaths annually from dieselgate in Europe - International Institute for Applied Systems Analysis, (2017). https://iiasa.ac.at/web/home/about/news/170918-diesel-nox.html (accessed July 5, 2021).

[8]   J. Balbuena, M. Cruz-Yusta, L. Sánchez, Nanomaterials to Combat NOx Pollution, J. Nanosci. Nanotechnol. 15 (2015) 6373–6385. doi:10.1166/jnn.2015.10871.

[9]   V. Nguyen, J. Che-Chin Yu, C. Huang, J.C.-S. Wu, Recent advances in the development of photocatalytic NOx abatement, in: Curr. Dev. Photocatal. Photocatalytic Mater., Elsevier, 2020: pp. 211–229. doi:10.1016/B978-0-12-819000-5.00014-X.

[10]   Q. Guo, C. Zhou, Z. Ma, X. Yang, Fundamentals of TiO$_2$ Photocatalysis: Concepts, Mechanisms, and Challenges, Adv. Mater. 31 (2019) 1–26. doi:10.1002/adma.201901997.

[11]   J.M. Cordero, R. Hingorani, E. Jimenez-Relinque, M. Grande, R. Borge, A. Narros, M. Castellote, NO$_X$ removal efficiency of urban photocatalytic pavements at pilot scale, Sci. Total Environ. 719 (2020) 137459. doi:10.1016/j.scitotenv.2020.137459.

[12]   A. Speziale, J.F. González-Sánchez, B. Taşcı, A. Pastor, L. Sánchez, C. Fernández-

Acevedo, T. Oroz-Mateo, C. Salazar, I. Navarro-Blasco, J.M. Fernández, J.I.
Alvarez, Development of Multifunctional Coatings for Protecting Stones and Lime
Mortars of the Architectural Heritage, Int. J. Archit. Herit. 3058 (2020) 1–22.
doi:10.1080/15583058.2020.1728594.

[13]   G.L. Guerrini, Photocatalytic performances in a city tunnel in Rome: NO_x
monitoring results, Constr. Build. Mater. 27 (2012) 165–175.
doi:10.1016/j.conbuildmat.2011.07.065.

[14]   J. Schneider, M. Matsuoka, M. Takeuchi, J. Zhang, Y. Horiuchi, M. Anpo, D.W.
Bahnemann, Understanding TiO_2 Photocatalysis: Mechanisms and Materials,
Chem. Rev. 114 (2014) 9919–9986. doi:10.1021/cr5001892.

[15]   J.Z. Bloh, A. Folli, D.E. Macphee, Photocatalytic NO_x abatement: Why the
selectivity matters, RSC Adv. 4 (2014) 45726–45734. doi:10.1039/c4ra07916g.

[16]   J. Balbuena, M. Cruz-Yusta, A. Pastor, L. Sánchez, α-Fe_2O_3/SiO_2 composites for the
enhanced photocatalytic NO oxidation, J. Alloys Compd. 735 (2018) 1553–1561.
doi:10.1016/j.jallcom.2017.11.259.

[17]   European Union law - Document 32020R0217, (n.d.). https://eur-
lex.europa.eu/legal-
content/EN/TXT/?uri=uriserv:OJ.L_.2020.044.01.0001.01.ENG&toc=OJ:L:2020:04
4:TOC (accessed July 5, 2021).

[18]   J. Balbuena, M. Cruz-Yusta, A.L. Cuevas, F. Martín, A. Pastor, R. Romero, L.
Sánchez, Hematite porous architectures as enhanced air purification
photocatalyst, J. Alloys Compd. 797 (2019) 166–173.
doi:10.1016/j.jallcom.2019.05.113.

[19]   Z. Wang, Y. Huang, M. Chen, X. Shi, Y. Zhang, J. Cao, W. Ho, S.C. Lee, Roles of N-

Vacancies over Porous g-C$_3$N$_4$ Microtubes during Photocatalytic NO$_x$ Removal, ACS Appl. Mater. Interfaces. 11 (2019) 10651–10662. doi:10.1021/acsami.8b21987.

[20]   M. Irfan, M. Sevim, Y. Koçak, M. Balci, Ö. Metin, E. Ozensoy, Enhanced photocatalytic NOx oxidation and storage under visible-light irradiation by anchoring Fe$_3$O$_4$ nanoparticles on mesoporous graphitic carbon nitride (mpg-C$_3$N$_4$), Appl. Catal. B Environ. 249 (2019) 126–137. doi:10.1016/j.apcatb.2019.02.067.

[21]   C. Wang, M. Fu, J. Cao, X. Wu, X. Hu, F. Dong, BaWO$_4$/g-C$_3$N$_4$ heterostructure with excellent bifunctional photocatalytic performance, Chem. Eng. J. 385 (2020) 123833. doi:10.1016/j.cej.2019.123833.

[22]   Y. Ye, Z. Zang, T. Zhou, F. Dong, S. Lu, X. Tang, W. Wei, Y. Zhang, Theoretical and experimental investigation of highly photocatalytic performance of CuInZnS nanoporous structure for removing the NO gas, J. Catal. 357 (2018) 100–107. doi:10.1016/j.jcat.2017.11.002.

[23]   Q. Zhang, Y. Huang, S. Peng, Y. Zhang, Z. Shen, J. Cao, W. Ho, S.C. Lee, D.Y.H. Pui, Perovskite LaFeO$_3$ -SrTiO$_3$ composite for synergistically enhanced NO removal under visible light excitation, Appl. Catal. B Environ. 204 (2017) 346–357. doi:10.1016/j.apcatb.2016.11.052.

[24]   Y. Huang, Y. Gao, Q. Zhang, Y. Zhang, J. ji Cao, W. Ho, S.C. Lee, Biocompatible FeOOH-Carbon quantum dots nanocomposites for gaseous NOx removal under visible light: Improved charge separation and High selectivity, J. Hazard. Mater. 354 (2018) 54–62. doi:10.1016/j.jhazmat.2018.04.071.

[25]   A. Gasparotto, G. Carraro, C. Maccato, C. Sada, J. Balbuena, M. Cruz-Yusta, L.

Sánchez, N. Vodišek, U. Lavrencic Štangar, D. Barreca, WO_3 -decorated ZnO

nanostructures for light-activated applications, CrystEngComm. 20 (2018) 1282–

1290. doi:10.1039/C7CE02148H.

[26]   A. Pastor, J. Balbuena, M. Cruz-Yusta, I. Pavlovic, L. Sánchez, ZnO on rice husk: A

sustainable photocatalyst for urban air purification, Chem. Eng. J. 368 (2019)

659–667. doi:10.1016/j.cej.2019.03.012.

[27]   Y. Lu, Y. Huang, Y. Zhang, T. Huang, H. Li, J. ji Cao, W. Ho, Effects of H_2O_2

generation over visible light-responsive $Bi/Bi_2O_{2-x}CO_3$ nanosheets on their

photocatalytic NO_x removal performance, Chem. Eng. J. 363 (2019) 374–382.

doi:10.1016/j.cej.2019.01.172.

[28]   J. Zhang, G. Zhu, S. Li, F. Rao, Q.-U. Hassan, J. Gao, Y. Huang, M. Hojamberdiev,

Novel $Au/La-Bi_5O_7I$ Microspheres with Efficient Visible-Light Photocatalytic

Activity for NO Removal: Synergistic Effect of Au Nanoparticles, La Doping, and

Oxygen Vacancy, ACS Appl. Mater. Interfaces. 11 (2019) 37822–37832.

doi:10.1021/acsami.9b14300.

[29]   M. Ran, H. Wang, W. Cui, J. Li, P. Chen, Y. Sun, J. Sheng, Y. Zhou, Y. Zhang, F.

Dong, Light-Induced Generation and Regeneration of Oxygen Vacancies in $BiSbO_4$

for Sustainable Visible Light Photocatalysis, ACS Appl. Mater. Interfaces. 11

(2019) 47984–47991. doi:10.1021/acsami.9b18154.

[30]   S. Wang, X. Ding, N. Yang, G. Zhan, X. Zhang, G. Dong, L. Zhang, H. Chen, Insight

into the effect of bromine on facet-dependent surface oxygen vacancies

construction and stabilization of Bi_2MoO_6 for efficient photocatalytic NO removal,

Appl. Catal. B Environ. 265 (2020) 118585. doi:10.1016/j.apcatb.2019.118585.

[31]   F. Rodriguez-Rivas, A. Pastor, C. Barriga, M. Cruz-Yusta, L. Sánchez, I. Pavlovic, Zn-

Al layered double hydroxides as efficient photocatalysts for NOx abatement, Chem. Eng. J. 346 (2018) 151–158. doi:10.1016/j.cej.2018.04.022.

[32] F. Rodriguez-Rivas, A. Pastor, G. de Miguel, M. Cruz-Yusta, I. Pavlovic, L. Sánchez, Cr^{3+} substituted Zn-Al layered double hydroxides as UV–Vis light photocatalysts for NO gas removal from the urban environment, Sci. Total Environ. 706 (2020) 136009. doi:10.1016/j.scitotenv.2019.136009.

[33] A. Pastor, F. Rodriguez-Rivas, G. de Miguel, M. Cruz-Yusta, F. Martin, I. Pavlovic, L. Sánchez, Effects of Fe^{3+} substitution on Zn-Al layered double hydroxides for enhanced NO photochemical abatement, Chem. Eng. J. 387 (2020) 124110. doi:10.1016/j.cej.2020.124110.

[34] F. Cavani, F. Trifirò, A. Vaccari, Hydrotalcite-type anionic clays: Preparation, properties and applications., Catal. Today. 11 (1991) 173–301. doi:10.1016/0920-5861(91)80068-K.

[35] L. Mohapatra, K. Parida, A review on the recent progress, challenges and perspective of layered double hydroxides as promising photocatalysts, J. Mater. Chem. A. 4 (2016) 10744–10766. doi:10.1039/c6ta01668e.

[36] G. Zhang, X. Zhang, Y. Meng, G. Pan, Z. Ni, S. Xia, Layered double hydroxides-based photocatalysts and visible-light driven photodegradation of organic pollutants: A review, Chem. Eng. J. 392 (2019) 123684. doi:10.1016/j.cej.2019.123684.

[37] C.-W. Jeon, S.-S. Lee, I.-K. Park, Flexible Visible-Blind Ultraviolet Photodetectors Based on ZnAl-Layered Double Hydroxide Nanosheet Scroll, ACS Appl. Mater. Interfaces. 11 (2019) 35138–35145. doi:10.1021/acsami.9b12082.

[38] Y. Zhao, Y. Zhao, G.I.N. Waterhouse, L. Zheng, X. Cao, F. Teng, L.Z. Wu, C.H. Tung,

D. O'Hare, T. Zhang, Layered-Double-Hydroxide Nanosheets as Efficient Visible-Light-Driven Photocatalysts for Dinitrogen Fixation, Adv. Mater. 29 (2017) 1–10. doi:10.1002/adma.201703828.

[39] Y. Zhao, X. Jia, G.I.N. Waterhouse, L.Z. Wu, C.H. Tung, D. O'Hare, T. Zhang, Layered Double Hydroxide Nanostructured Photocatalysts for Renewable Energy Production, Adv. Energy Mater. 6 (2016) 1–20. doi:10.1002/aenm.201501974.

[40] C. Chen, A. Wangriya, J.-C. Buffet, D. O'Hare, Tuneable ultra high specific surface area Mg/Al-CO_3 layered double hydroxides, Dalt. Trans. 44 (2015) 16392–16398. doi:10.1039/C5DT02641E.

[41] Q. Wang, D. O'Hare, Recent Advances in the Synthesis and Application of Layered Double Hydroxide (LDH) Nanosheets, Chem. Rev. 112 (2012) 4124–4155. doi:10.1021/cr200434v.

[42] Q. Wang, D. O'Hare, Large-scale synthesis of highly dispersed layered double hydroxide powders containing delaminated single layer nanosheets, Chem. Commun. 49 (2013) 6301. doi:10.1039/c3cc42918k.

[43] C. Chen, M. Yang, Q. Wang, J.-C. Buffet, D. O'Hare, Synthesis and characterisation of aqueous miscible organic-layered double hydroxides, J. Mater. Chem. A. 2 (2014) 15102–15110. doi:10.1039/C4TA02277G.

[44] J.-C. Buffet, Z.R. Turner, R.T. Cooper, D. O'Hare, Ethylene polymerisation using solid catalysts based on layered double hydroxides, Polym. Chem. 6 (2015) 2493–2503. doi:10.1039/C4PY01742K.

[45] Q. Yan, Y. Nie, R. Yang, Y. Cui, D. O'Hare, Q. Wang, Highly dispersed Cu_yAlO_x mixed oxides as superior low-temperature alkali metal and SO_2 resistant NH_3-SCR catalysts, Appl. Catal. A Gen. 538 (2017) 37–50.

doi:10.1016/j.apcata.2017.03.021.

[46] L. Qiu, Y. Gao, C. Zhang, Q. Yan, D. O'Hare, Q. Wang, Synthesis of highly efficient flame retardant polypropylene nanocomposites with surfactant intercalated layered double hydroxides, Dalt. Trans. 47 (2018) 2965–2975. doi:10.1039/c7dt03477f.

[47] S. Shang, A. Hanif, M. Sun, Y. Tian, Y.S. Ok, I.K.M. Yu, D.C.W. Tsang, Q. Gu, J. Shang, Novel M (Mg/Ni/Cu)-Al-CO_3 layered double hydroxides synthesized by aqueous miscible organic solvent treatment (AMOST) method for CO_2 capture, J. Hazard. Mater. 373 (2019) 285–293. doi:10.1016/j.jhazmat.2019.03.077.

[48] I.K.M. Yu, A. Hanif, D.C.W. Tsang, J. Shang, Z. Su, H. Song, Y.S. Ok, C.S. Poon, Tuneable functionalities in layered double hydroxide catalysts for thermochemical conversion of biomass-derived glucose to fructose, Chem. Eng. J. 383 (2020) 122914. doi:10.1016/j.cej.2019.122914.

[49] U. Costantino, F. Marmottini, M. Nocchetti, R. Vivani, New Synthetic Routes to Hydrotalcite-Like Compounds – Characterisation and Properties of the Obtained Materials, Eur. J. Inorg. Chem. 1998 (1998) 1439–1446. doi:10.1002/(SICI)1099-0682(199810)1998:10<1439::AID-EJIC1439>3.0.CO;2-1.

[50] W.H. Zhang, X.D. Guo, J. He, Z.Y. Qian, Preparation of Ni(II)/Ti(IV) layered double hydroxide at high supersaturation, J. Eur. Ceram. Soc. 28 (2008) 1623–1629. doi:10.1016/j.jeurceramsoc.2007.11.016.

[51] G. Lin, L. Zhu, T. Duan, L. Zhang, B. Liu, J. Lei, Efficient capture of iodine by a polysulfide-inserted inorganic NiTi-layered double hydroxides, Chem. Eng. J. 378 (2019) 122181. doi:10.1016/j.cej.2019.122181.

[52] C. Chen, M. Yang, Q. Wang, J.-C. Buffet, D. O'Hare, SI - Synthesis and

characterisation of aqueous miscible organic-layered double hydroxides, J. Mater. Chem. A. 2 (2014) 15102–15110. doi:10.1039/C4TA02277G.

[53]   K. Cermelj, K. Ruengkajorn, J.C. Buffet, D. O'Hare, Layered double hydroxide nanosheets via solvothermal delamination, J. Energy Chem. 35 (2019) 88–94. doi:10.1016/j.jechem.2018.11.008.

[54]   V. Rives, Layered Double Hydroxides: Present and Future, Nova Science Publishers Inc, New York, 2001.

[55]   M.C. Capel-Sanchez, G. Blanco-Brieva, J.M. Campos-Martin, M.P. de Frutos, W. Wen, J.A. Rodriguez, J.L.G. Fierro, Grafting Strategy to Develop Single Site Titanium on an Amorphous Silica Surface, Langmuir. 25 (2009) 7148–7155. doi:10.1021/la900578u.

[56]   Y. Zhao, B. Li, Q. Wang, W. Gao, C.J. Wang, M. Wei, D.G. Evans, X. Duan, D. O'Hare, NiTi-Layered double hydroxides nanosheets as efficient photocatalysts for oxygen evolution from water using visible light, Chem. Sci. 5 (2014) 951–958. doi:10.1039/C3SC52546E.

[57]   J. Cai, Y. Zhang, Y. Qian, C. Shan, B. Pan, Enhanced Defluoridation Using Novel Millisphere Nanocomposite of La-Doped Li-Al Layered Double Hydroxides Supported by Polymeric Anion Exchanger, Sci. Rep. 8 (2018) 11741. doi:10.1038/s41598-018-29497-1.

[58]   X. Wu, R. Wang, Y. Du, X. Li, H. Meng, X. Xie, NO_x removal by selective catalytic reduction with ammonia over hydrotalcite-derived NiTi mixed oxide, New J. Chem. 43 (2019) 2640–2648. doi:10.1039/c8nj05280h.

[59]   Y. Zhao, P. Chen, B. Zhang, D.S. Su, S. Zhang, L. Tian, J. Lu, Z. Li, X. Cao, B. Wang, M. Wei, D.G. Evans, X. Duan, Highly dispersed TiO_6 units in a layered double

hydroxide for water splitting, Chem. - A Eur. J. 18 (2012) 11949–11958. doi:10.1002/chem.201201065.

[60] Y. Lu, J.H. Warner, Synthesis and Applications of Wide Bandgap 2D Layered Semiconductors Reaching the Green and Blue Wavelengths, ACS Appl. Electron. Mater. 2 (2020) 1777–1814. doi:10.1021/acsaelm.0c00105.

[61] J. Ângelo, L. Andrade, L.M. Madeira, A. Mendes, An overview of photocatalysis phenomena applied to NO_x abatement, J. Environ. Manage. 129 (2013) 522–539. doi:10.1016/j.jenvman.2013.08.006.

[62] W. Cui, J. Li, F. Dong, Y. Sun, G. Jiang, W. Cen, S.C. Lee, Z. Wu, Highly Efficient Performance and Conversion Pathway of Photocatalytic NO Oxidation on SrO-Clusters@Amorphous Carbon Nitride, Environ. Sci. Technol. 51 (2017) 10682–10690. doi:10.1021/acs.est.7b00974.

[63] R.J.L. N.I. Sax, Sax's Dangerous Properties of Industrial Materials, 12th ed, Van Nostrand Reinhold, New York, 2012.

[64] Y. Wang, H. Huang, J. Gao, G. Lu, Y. Zhao, Y. Xu, L. Jiang, TiO_2–SiO_2 composite fibers with tunable interconnected porous hierarchy fabricated by single-spinneret electrospinning toward enhanced photocatalytic activity, J. Mater. Chem. A. 2 (2014) 12442–12448. doi:10.1039/C4TA01208A.

[65] J. Balbuena, J.M. Calatayud, M. Cruz-Yusta, P. Pardo, F. Martín, J. Alarcón, L. Sánchez, Mesocrystalline anatase nanoparticles synthesized using a simple hydrothermal approach with enhanced light harvesting for gas-phase reaction, Dalt. Trans. 47 (2018) 6590–6597. doi:10.1039/C8DT00721G.

[66] X. Lv, J. Zhang, X. Dong, J. Pan, W. Zhang, W. Wang, G. Jiang, F. Dong, Layered double hydroxide nanosheets as efficient photocatalysts for NO removal: Band

structure engineering and surface hydroxyl ions activation, Appl. Catal. B Environ. 277 (2020) 119200. doi:10.1016/j.apcatb.2020.119200.

[67] W. Zhang, X. Dong, Y. Liang, Y. Sun, F. Dong, Ag/AgCl nanoparticles assembled on $BiOCl/Bi_{12}O_{17}Cl_2$ nanosheets: Enhanced plasmonic visible light photocatalysis and in situ DRIFTS investigation, Appl. Surf. Sci. 455 (2018) 236–243. doi:10.1016/j.apsusc.2018.05.171.

[68] P. Chen, H. Liu, Y. Sun, J. Li, W. Cui, L. Wang, W. Zhang, X. Yuan, Z. Wang, Y. Zhang, F. Dong, Bi metal prevents the deactivation of oxygen vacancies in $Bi_2O_2CO_3$ for stable and efficient photocatalytic NO abatement, Appl. Catal. B Environ. 264 (2020) 118545. doi:10.1016/j.apcatb.2019.118545.

[69] J. Liao, W. Cui, J. Li, J. Sheng, H. Wang, X. Dong, P. Chen, G. Jiang, Z. Wang, F. Dong, Nitrogen defect structure and NO+ intermediate promoted photocatalytic NO removal on H_2 treated $g-C_3N_4$, Chem. Eng. J. 379 (2020) 122282. doi:10.1016/j.cej.2019.122282.

[70] W. Huo, T. Cao, W. Xu, Z. Guo, X. Liu, H.C. Yao, Y. Zhang, F. Dong, Facile construction of $Bi_2Mo_3O_{12}@Bi_2O_2CO_3$ heterojunctions for enhanced photocatalytic efficiency toward NO removal and study of the conversion process, Chinese J. Catal. 41 (2020) 268–275. doi:10.1016/S1872-2067(19)63460-1.

[71] X. Li, W. Zhang, W. Cui, J. Li, Y. Sun, G. Jiang, H. Huang, Y. Zhang, F. Dong, Reactant activation and photocatalysis mechanisms on $Bi-metal@Bi_2GeO_5$ with oxygen vacancies: A combined experimental and theoretical investigation, Chem. Eng. J. 370 (2019) 1366–1375. doi:10.1016/j.cej.2019.04.003.

[72] W. Huo, W. Xu, T. Cao, X. Liu, Y. Zhang, F. Dong, Carbonate-intercalated defective

bismuth tungstate for efficiently photocatalytic NO removal and promotion

mechanism study, Appl. Catal. B Environ. 254 (2019) 206–213.

doi:10.1016/j.apcatb.2019.04.099.
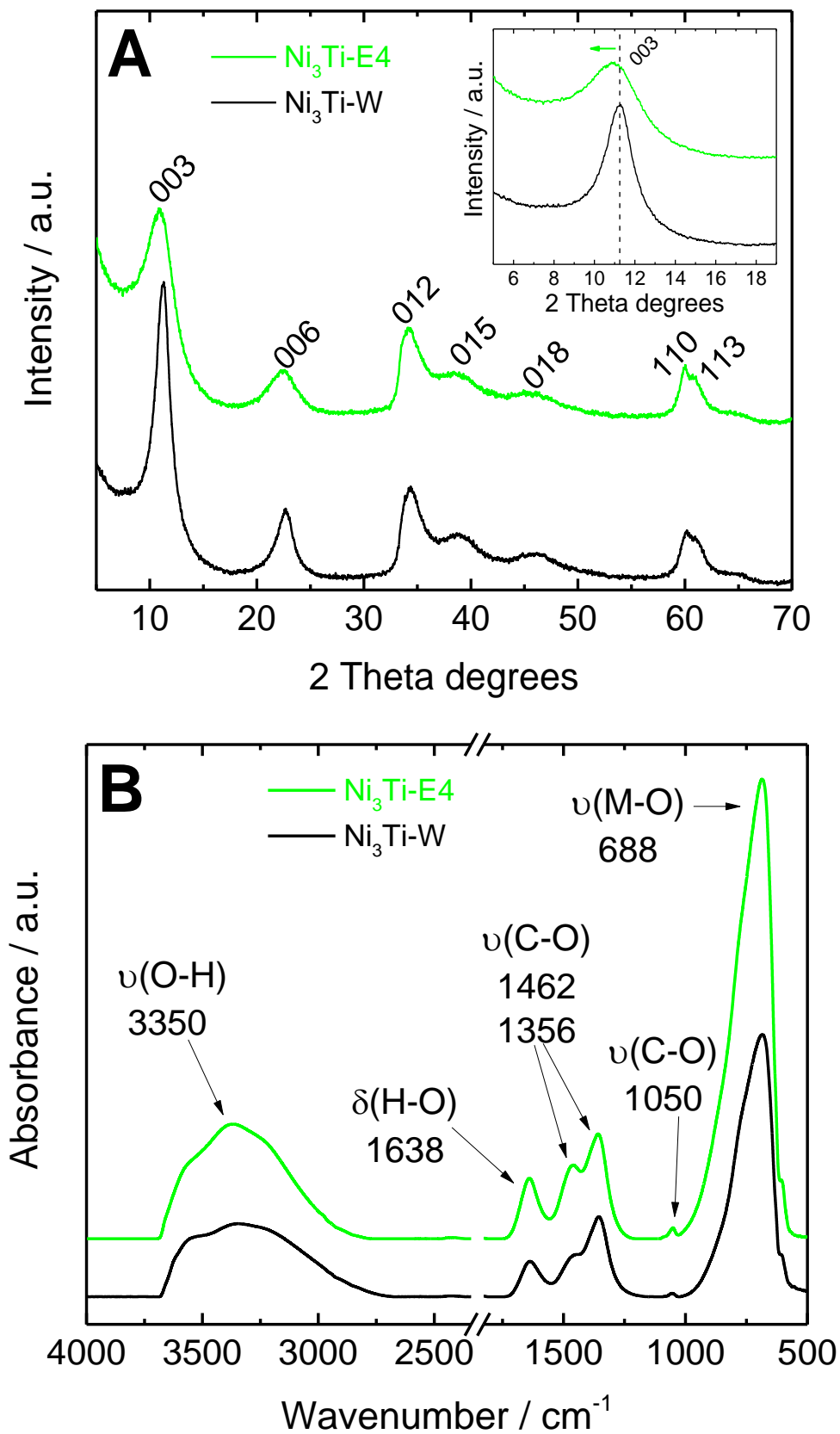
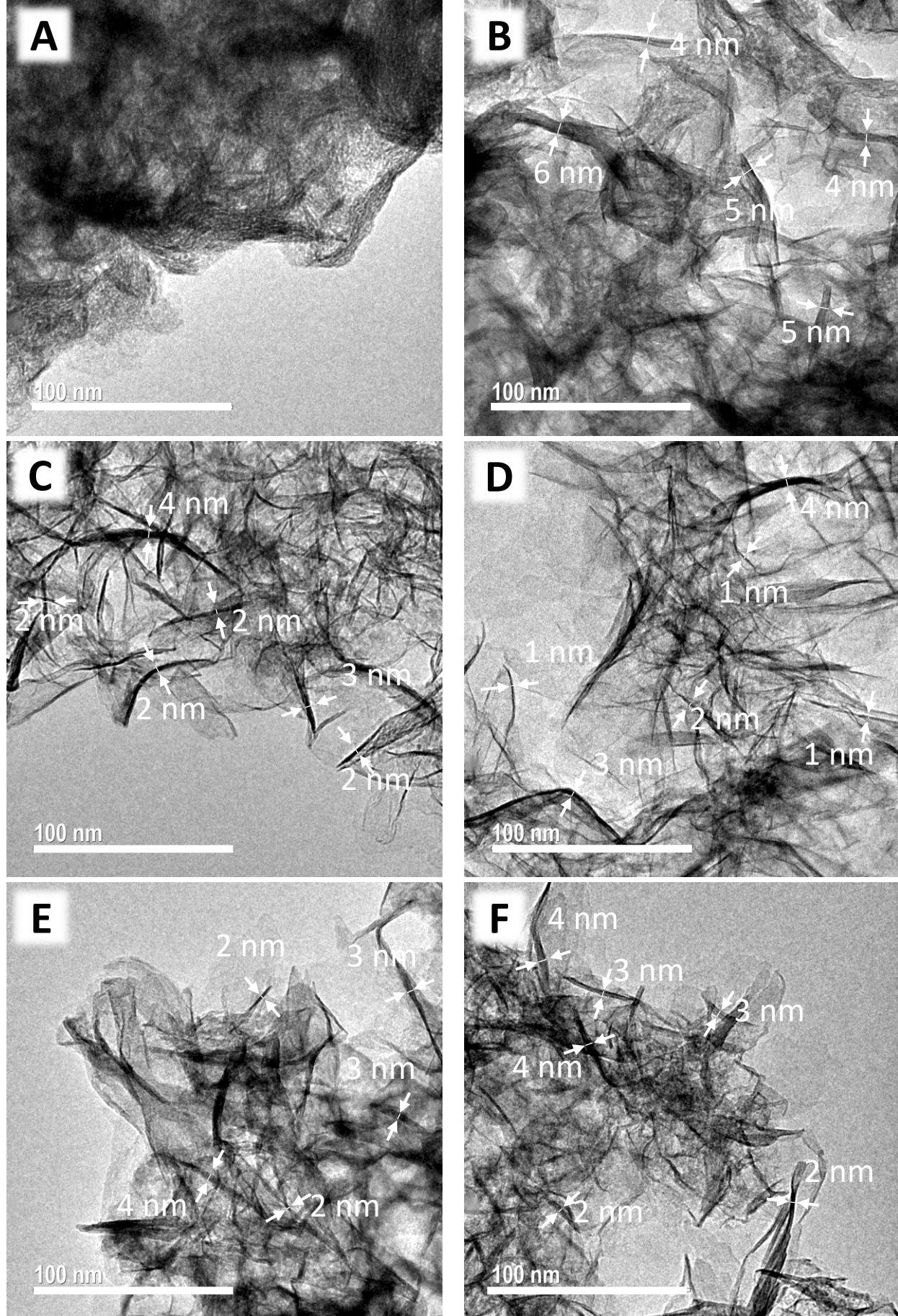**Fig. 1.** (A) XRD patterns and (B) ATR spectra for Ni_3Ti samples.

Fig. 2. TEM images of: (A) Ni$_3$Ti-W; Ni$_3$Ti with different redispersion times in the AMOST: (B) 2 h, (C) 4 h, (D) 6 h, (E) 24 h, (F) 48 h.
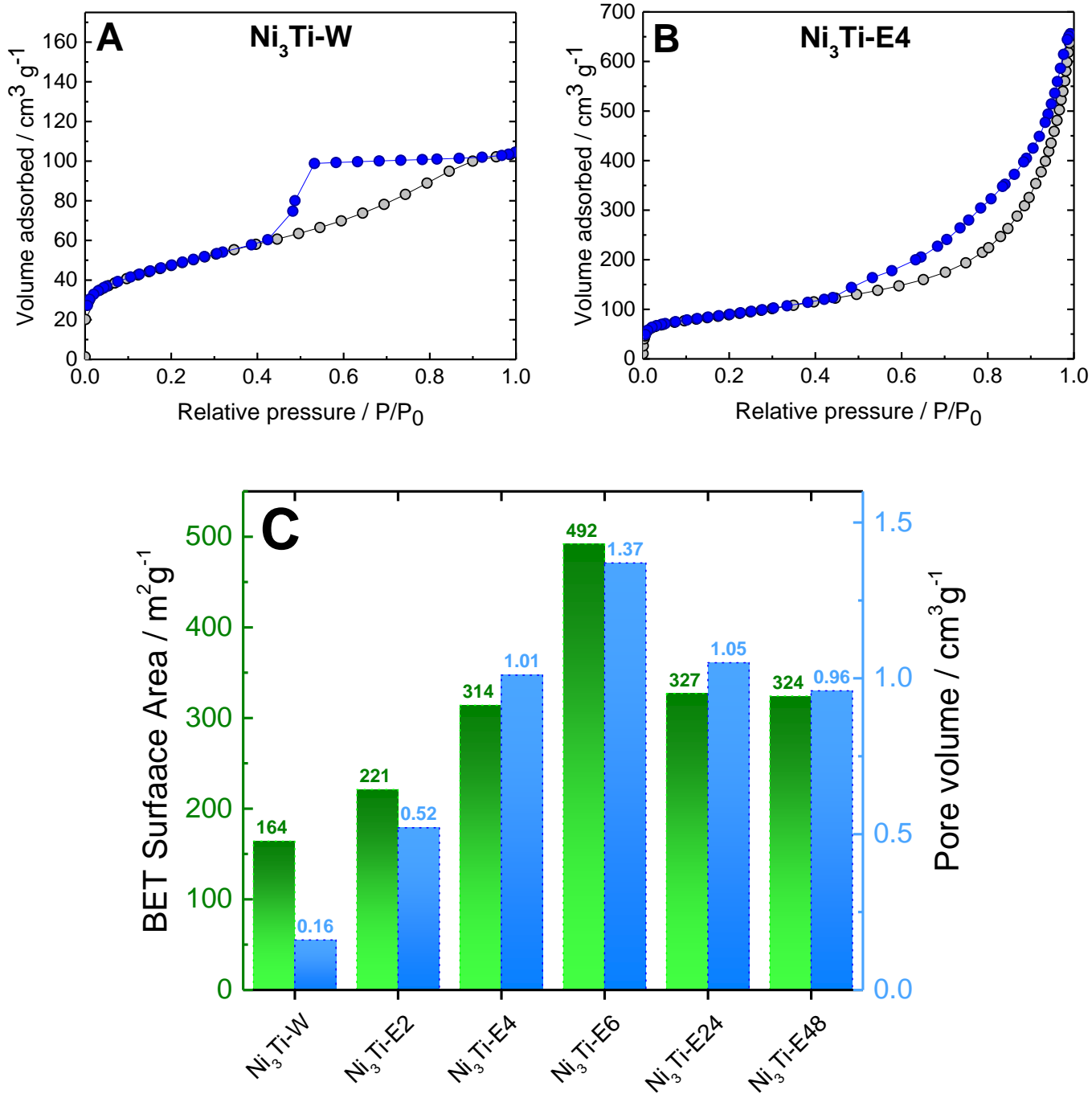
Fig. 3. (A, B) N_2 adsorption-desorption isotherms of Ni_3Ti samples. (C) BET surface area and pore volume for Ni_3Ti with different redispersion times in the AMOST.
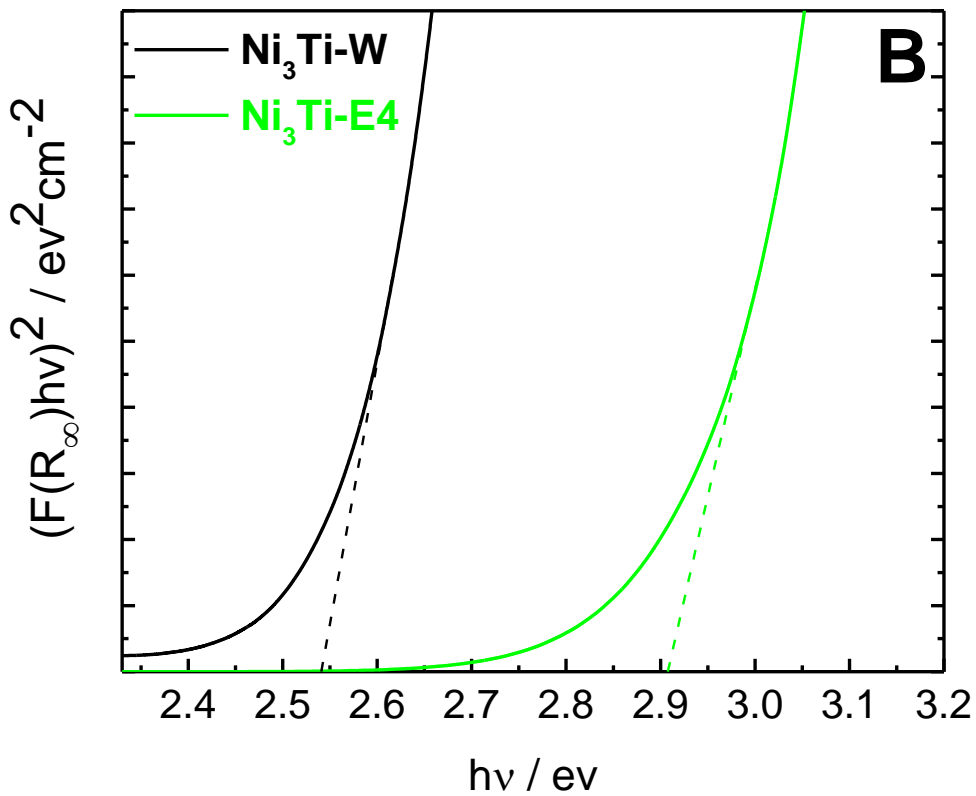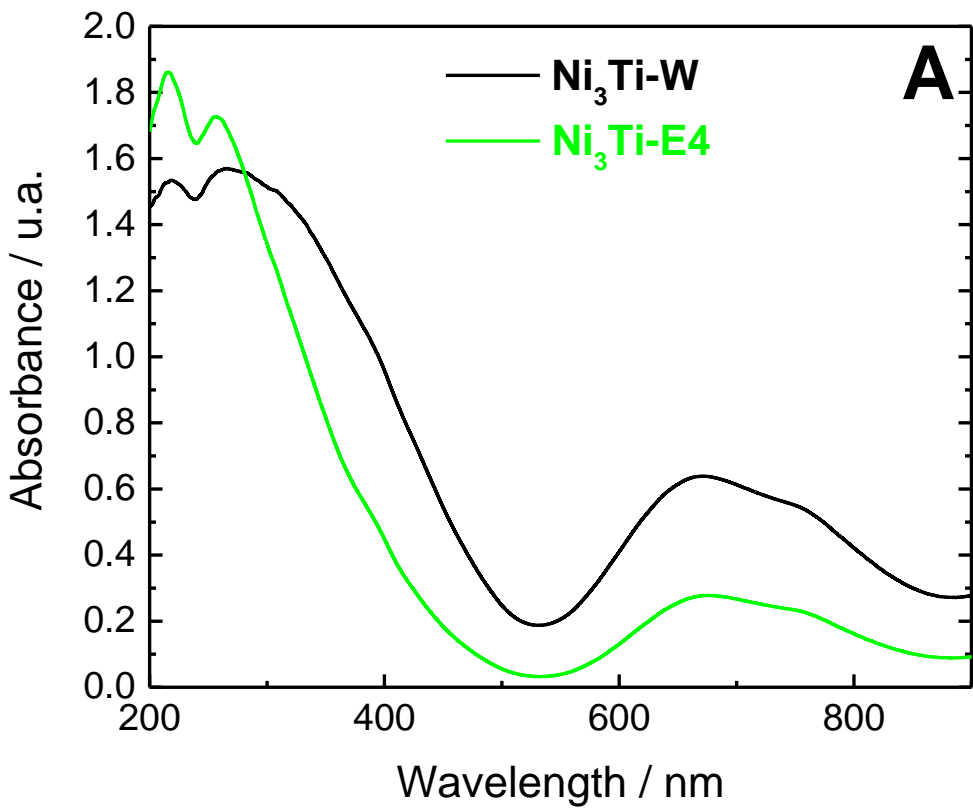
Fig. 4. (A) UV–Vis absorption spectra and (B) Kubelka-Munk transformed function plots for Ni_3Ti-W and Ni_3Ti-E4 samples.
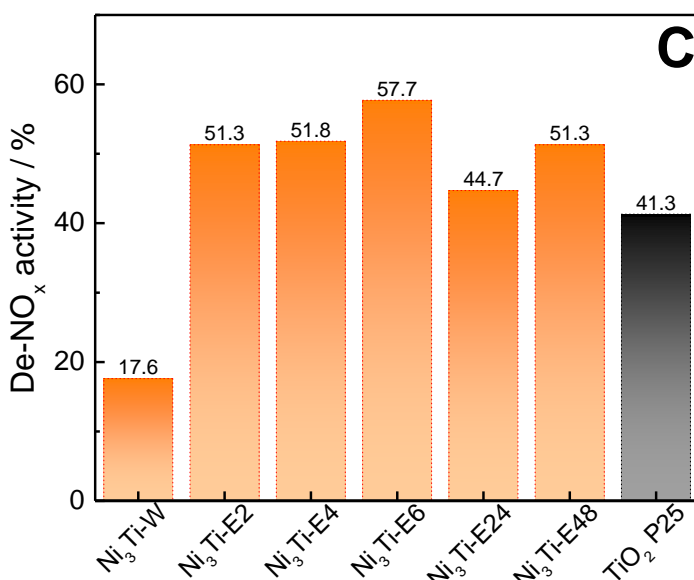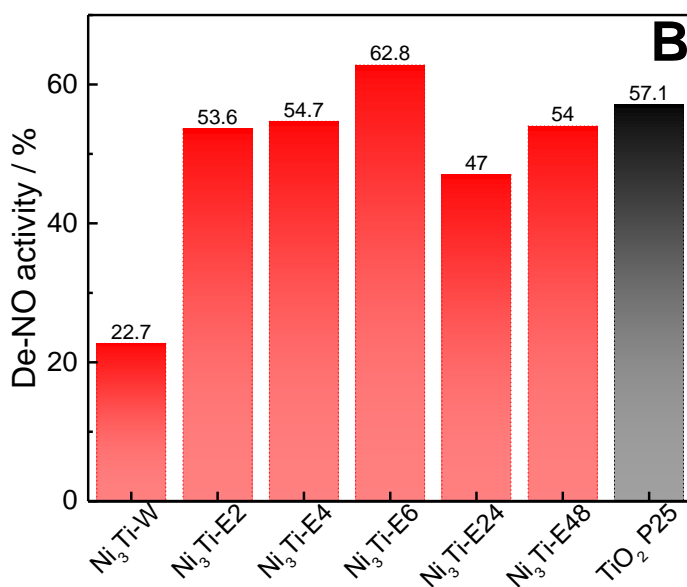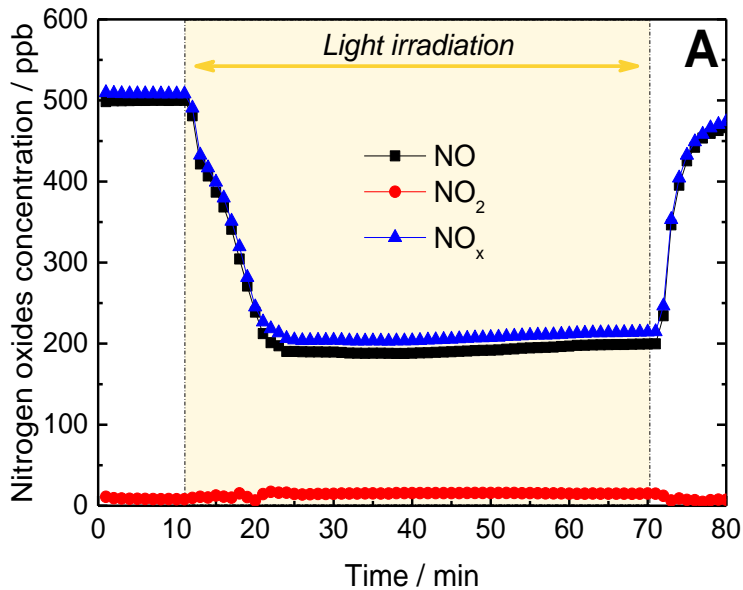
Fig. 5. (A) Nitrogen oxides concentration profile obtained during the photocatalytic NO removal test on Ni₃Ti-E4 sample; (B) calculated De-NO and (C) De-NOx indexes for Ni₃Ti with different redispersion times in the AMOST and TiO₂ P25.
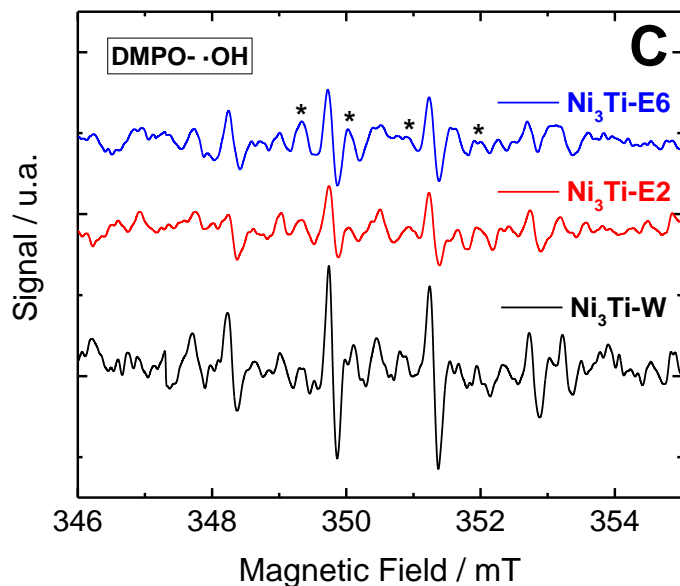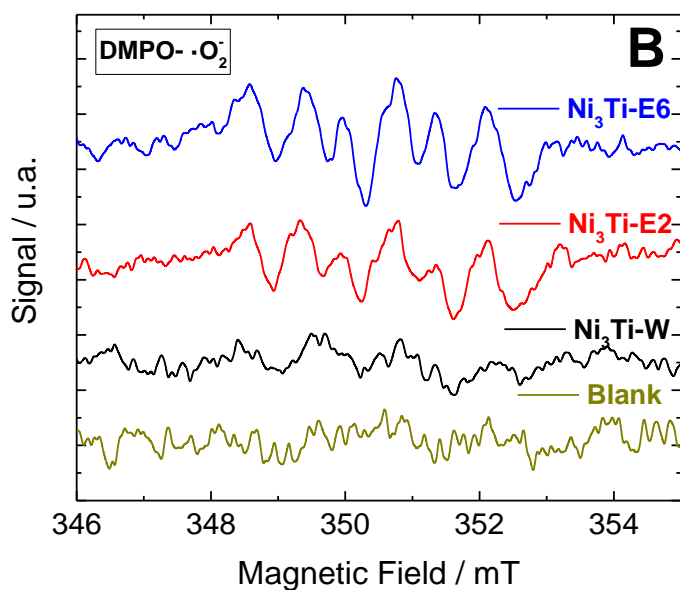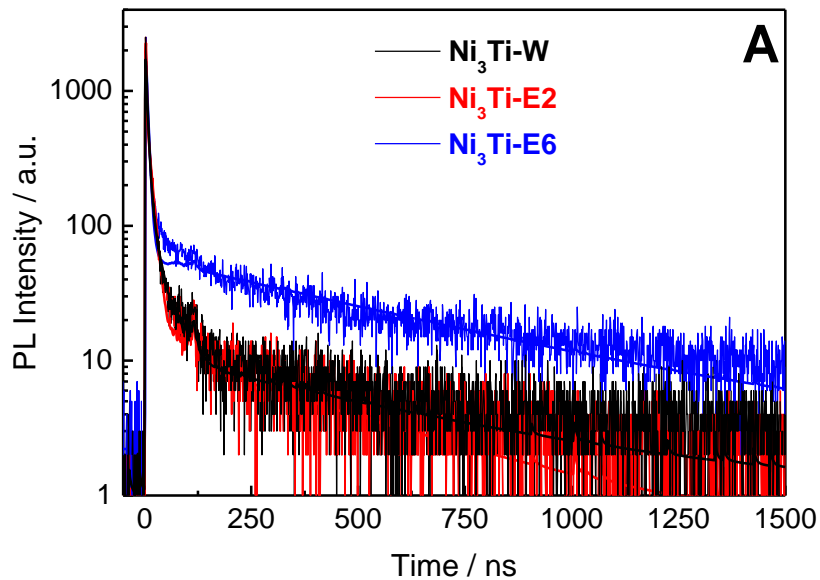
Fig. 6. (A) Time decay of the photoluminescence signals and (B, C) DMPO spin-trapping EPR spectra for the Ni$_3$Ti-W, Ni$_3$Ti-E2 and Ni$_3$Ti-E6 photocatalysts.
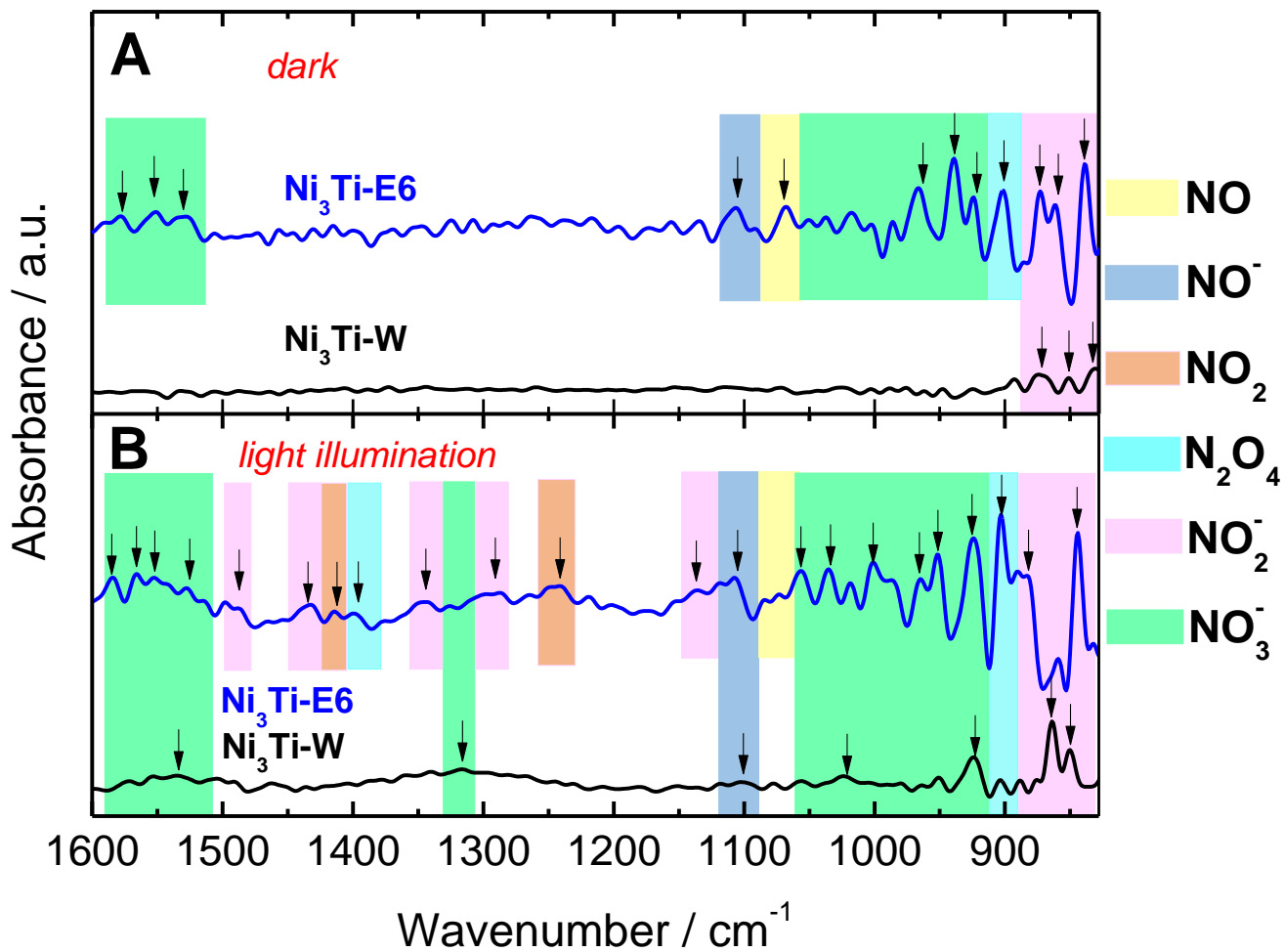
Fig. 7. In situ DRIFTS spectra obtained while NO and O_2 gases are flowing through the Ni_3Ti-W and Ni_3Ti-E6 samples in (A) dark conditions and (B) under light illumination.